Mechanical Systems and Signal Processing 161 (2021) 107960

Contents lists available at ScienceDirect

Mechanical Systems and Signal Processing

journal homepage: www.elsevier.com/locate/ymssp

Online parameter estimation under non-persistent excitations for high-rate dynamic systems

Jin Yan [a,*], Simon Laflamme [b], Jonathan Hong [c], Jacob Dodson [d]

[a] Department of Civil, Construction, and Environmental Engineering, Iowa State University, Ames, IA, USA; Palo Alto Research Center, Palo Alto, CA, USA
[b] Department of Electrical and Computer Engineering, Iowa State University, Ames, IA, USA
[c] Applied Research Associates, Valparaiso, FL, USA
[d] Air Force Research Laboratory, Munitions Directorate, Eglin AFB, FL, USA

ARTICLE INFO

Article history:
Received 28 October 2020
Accepted 6 April 2021

Communicated by Yoram Halevi

Keywords:
High-rate
System identification
Real-time
Adaptive system
Concurrent learning

ABSTRACT

High-rate dynamic systems are defined as systems experiencing dynamic events of typical amplitudes higher than 100 g_n for a duration of less than 100 ms. They are characterized by 1) large uncertainties on the external loads; 2) high levels of nonstationarity and heavy disturbance; and 3) generation of unmodeled dynamics from changes in mechanical configuration. To fully enable these systems, feedback capabilities must be developed. This includes computationally fast software and low latency hardware. This paper presents a pure time-based online parameter estimation algorithm for high-rate dynamic systems with real-time applicability. The algorithm is based on a model reference adaptive system architecture consisting of a reference system and an adaptive model. The adaptive model is built on a reduced order physical representation of the system and uncertainties are linearized. Uncertain coefficients are adapted leveraging instantaneous measurements and historical input–output data sets, termed history stack data, based on concurrent learning theory for coping with the lack of persistent excitation. The history stack is sequentially modified based on a singular value maximizing algorithm to accelerate convergence. The algorithm is numerically verified and experimentally validated on a testbed consisting of a cantilever beam with a moving cart. Numerical verifications show that the algorithm provides fast and accurate convergence when concurrent learning is used. Experimental validations show that the algorithm can successfully identify static positions of the cart, and can also track its movement relatively well, with large chattering and overshoots during travel time. The average computation speed of the algorithm per sample step, implemented in MATLAB, is 93 μs. It is envisioned that the implementation of the algorithm on an FPGA, along with refined coding, will greatly reduce computation time.

1. Introduction

Recent advances in technologies have empowered high-rate dynamic systems with new capabilities, enabling enhanced operations and field deployments. These systems, here defined as those experiencing dynamic events of typical amplitudes higher than 100 g_n for a duration of less than 100 ms, include active blast mitigation systems, advanced weaponry, and hypersonic vehicles [1]. Because of the harsh environments in which high-rate systems evolve, an important challenge is in design-

* Corresponding author at: 3333 Coyote Hill Rd, Palo Alto, CA 94304, USA.
E-mail address: yanjin@iastate.edu (J. Yan).

https://doi.org/10.1016/j.ymssp.2021.107960
0888-3270/

ing feedback systems capable of real-time decisions in order to ensure critical functionalities to preserve structural integrity and users' safety. However, these feedback systems are currently limited by computation time and mechanical latency.

Of interest to this paper is the development of system identification capabilities in the high-rate realm. Note that the term high-rate relates to sub-millisecond feedback requirements, not to the dynamic properties of the engineering system itself. There are several challenges associated with high-rate systems: 1) large uncertainties on the external loads; 2) high levels of nonstationarity and heavy disturbance; and 3) generation of unmodeled dynamics from changes in mechanical configuration [1]. A successful algorithm for high-rate systems is one capable of rapidly detecting and quantifying damages, learning from input–output data, ensuring robustness to sensor noise and unmodeled dynamics, and adapting to changes in the environment [2]. In the introductory paper on high-rate state estimation [1], it was argued that the general class of adaptive observers and estimators offers a path to producing microsecond convergence rates, but that their accuracy comes at higher computation costs. The authors have studied adaptive data-based techniques for real-time state estimation based on a sequential neural network with a self-organizing input space [3]. While the data-based technique showed great promise at high-rate state estimation, it did not provide insights into the system's physical characteristics, as it is generally the case for data-based techniques.

A solution is to integrate physical knowledge in order to produce physical state estimation capabilities. Such techniques for real-time applications include time–frequency and Bayesian methods. For example, [4] tracks time-varying frequency to detect the progressive degradation of motor bearing using time–frequency transforms, and [5] developed an adaptive sparse time–frequency analysis method that estimates the instantaneous frequency of tensioned bridge cables. Generally, frequency-based techniques only produce physical information at the global (i.e., structure) level, and more complex/computationally expensive signal processing is required for further damage assessment and localization. Alternatively, Bayesian approximation techniques have been studied [6,7] due to their capabilities to locate damage [8]. They have been applied, for example, to real-time fatigue crack growth monitoring and characterization [9,10]. While promising, nonlinearities and non-Gaussian distributions of the probability density of the states may limit the application of these techniques.

Alternatively, methods based on model reference adaptive systems (MRAS) [11] have shown great promise at handling nonlinearities, uncertainties, and perturbations. MRAS consists of adaptive algorithms designed to minimize the discrepancies between the reference model and the adaptive model. Examples of MRAS-based algorithms include disturbance observers [12] and sliding mode observers [13]. MRAS has been applied to high-rate systems in [14]. The algorithm consisted of identifying, online, the position of a moving cart on a cantilever beam through the adaptive identification of the system's fundamental frequency using a sliding mode observer. Experimental data for the moving cart was generated on a new testbed termed DROPBEAR (Dynamic Reproduction of Projectiles in Ballistic Environments for Advanced Research). DROPBEAR was used in [15] to validate a real-time system identification algorithm experimentally using a field-programmable gate array (FPGA). The algorithm consisted of identifying the system's fundamental frequency, related to the cart position, by matching extracted frequencies to pre-generated finite element models within 202 ms with a 4.04 ms processing time per step. The testbed data was also used in [16] for validating a sensor network design methodology based on model updating using a sliding mode observer.

A common challenge in applying state estimators to high-rate systems is in the lack of persistent excitations, where convergence to the correct state cannot be guaranteed [17]. Joyce et al. [18] investigated the tradeoffs between robustness, noise, and convergence speed for high-rate systems and discussed the need for persistently exciting inputs. Algorithms have been developed to improve the robustness of parameter convergence in such operating regimes characterized by high impact forces, heavy noise, and fast convergence speed requirements. This can be done through the modification of the adaptive law [19], and relaxing the restriction on the persistence of the excitation with concurrent learning (CL) [20]. CL consists of concurrently using real-time measurements augmented with a temporally limited historical data set to guarantee exponential convergence. The concept of CL for non-persistent excitations has also been studied in [21,22].

In this paper, a time-based state estimator for high-rate systems with non-persistent excitations is developed and applied to the online identification of the position of a sliding cart using the DROPBEAR testbed. The algorithm is based on an MRAS architecture consisting of a reference system and an adaptive model. The adaptive model is built on a reduced order physical representation of the system. Uncertainties in the system are written as basis functions of unknown coefficients. These coefficients are adapted leveraging instantaneous measurements and historical input–output data sets, termed history stack data, based on CL theory. The history stack is sequentially modified based on a singular value maximizing algorithm to accelerate computation time with respect to a batch process.

The rest of the paper is organized as follows. First, the background is provided on the testbed used to verify and validate the algorithm and on the construction of its reduced order physical representation, and the research problem is formulated. Second, the online parameter estimation algorithm is presented, which includes its adaptation law and stability analysis. Third, the algorithm is numerically verified for the identification of one and two unknown parameters for a single-degree-of-freedom (SDOF) system. Fourth, the algorithm is experimentally validated using testbed data. Lastly, the paper is concluded.

2. Background

This section provides the background on the DROPBEAR testbed, and on its physical representation and reduction into a lower order system. After, the parameterization of the uncertain system and the associated requirements on parameter estimation are introduced.

2.1. DROPBEAR Testbed

DROPBEAR is an experimental testbed designed in collaboration between the Air Force Research Laboratory and Michigan Technological University to validate online parameter estimation algorithms for high-rate dynamic systems [14]. Shown Fig. 1, the testbed features a cantilevered steel beam (505 mm in length) configuration with an electromagnet at the tip and a moveable cart. The electromagnet is an added mass that can be detached in real-time. The movable cart acts as a variable pin and is displaced along the beam with a linear actuator. These unique features provide repeatable, fast-changing dynamics that can be experienced during high-rate events, such as a sudden change in stiffness from damage, a gradual change in stiffness from changes in boundary conditions, or slow deformations in the system. To generate experimental data used in this research, one PCB 353B17 accelerometer was attached to the beam, 300 mm away from the clamp. A PCB 086C01 modal hammer was used to excite the beam, applied at the tip. A NI-9234 IEPE analog input module hosted in a NI cDAQ-9172 eight-slot chassis acquired data in the range of 25,000 Hz. In this study, the electromagnet is fixed at the tip of the beam, and various cart positions are evaluated: fixed at 50 mm, 100 mm, 150 mm, and 200 mm from the clamp, and moving back and forth from 50 mm to 200 mm from the clamp. Remark that such spatial variations in the cart position change the fundamental frequency of the system between 17.7 Hz and 31.0 Hz, which is deemed adequate to test high-rate state estimation algorithms. The construction of testbeds in the higher dynamic frequency ranges is left to future work.

2.2. Reduced order model

A physical representation of DROPBEAR was developed in [14]. Briefly, it has the form:

$$\mathbf{M}\ddot{\mathbf{x}}(t) + \mathbf{C}\dot{\mathbf{x}}(t) + \mathbf{K}\mathbf{x}(t) = \mathbf{r}(t) \tag{1}$$

where, for an n degree-of-freedom (nDOF) system, $\mathbf{M} \in \mathbb{R}^{n\times n}$ is the mass matrix, $\mathbf{C} \in \mathbb{R}^{n\times n}$ the damping matrix, $\mathbf{K} \in \mathbb{R}^{n\times n}$ the stiffness matrix, $\mathbf{r} \in \mathbb{R}^{n\times 1}$ the external excitation, $\mathbf{x} \in \mathbb{R}^{n\times n}$ the displacement vector, and the dot denotes a time derivative. A model reduction technique is applied based on the System Equivalent Reduction Expansion Process (SEREP) [23,24] to obtain a computationally faster physical representation. With SEREP, the full model (Eq. 1) is divided into master (subscript m) and slave (subscript s) DOFs, written:

$$\begin{bmatrix} \mathbf{M}_{mm} & \mathbf{M}_{ms} \\ \mathbf{M}_{sm} & \mathbf{M}_{ss} \end{bmatrix} \begin{bmatrix} \ddot{\mathbf{x}}_m(t) \\ \ddot{\mathbf{x}}_s(t) \end{bmatrix} + \begin{bmatrix} \mathbf{C}_{mm} & \mathbf{C}_{ms} \\ \mathbf{C}_{sm} & \mathbf{C}_{ss} \end{bmatrix} \begin{bmatrix} \dot{\mathbf{x}}_m(t) \\ \dot{\mathbf{x}}_s(t) \end{bmatrix} + \begin{bmatrix} \mathbf{K}_{mm} & \mathbf{K}_{ms} \\ \mathbf{K}_{sm} & \mathbf{K}_{ss} \end{bmatrix} \begin{bmatrix} \mathbf{x}_m(t) \\ \mathbf{x}_s(t) \end{bmatrix} = \begin{bmatrix} \mathbf{r}_m(t) \\ \mathbf{r}_s(t) \end{bmatrix} \tag{2}$$

Modal truncation is conducted using the first p eigenvectors, yielding an expression for $\mathbf{x}(t)$:

$$\mathbf{x}(t) = \mathbf{\Phi}\mathbf{q}(t) = \mathbf{\Phi}_p\mathbf{q}_p(t) \tag{3}$$

where $\mathbf{\Phi}$ is the full eigenvector matrix, $\mathbf{q}(\mathbf{t})$ is modal coordinates, and subscript p denotes the truncated quantities. Dividing the displacement vector into terms associated with the master and slave DOFs, Eq. (3) can be written:

$$\mathbf{x}(t) = \begin{bmatrix} \mathbf{x}_m(t) \\ \mathbf{x}_s(t) \end{bmatrix} = \begin{bmatrix} \mathbf{\Phi}_{mp} \\ \mathbf{\Phi}_{sp} \end{bmatrix} \mathbf{q}_p(t) \tag{4}$$

Eq. (4) describes displacement responses associated with the first p eigenvectors. Matrix $\mathbf{\Phi}_{mp}$ contains p eigenvectors of the master DOFs m, and matrix $\mathbf{\Phi}_{sp}$ contains p eigenvectors of the slave DOFs s. Matrix $\mathbf{\Phi}_{mp}$ is a square matrix when the measured/master DOFs are equal to the number of modes of interest ($m = p$). When $m > p$, Eq. (4) can be modified using:

$$\mathbf{y}_p(t) = \mathbf{\Phi}_{mp}^{\mathrm{T}}\mathbf{x}_m(t) = \mathbf{\Phi}_{mp}^{\mathrm{T}}\mathbf{\Phi}_{mp}\tilde{\mathbf{q}}_p(t) \tag{5}$$

where $\tilde{\mathbf{q}}_p(t)$ denotes an estimation of $\mathbf{q}_p(t)$, written

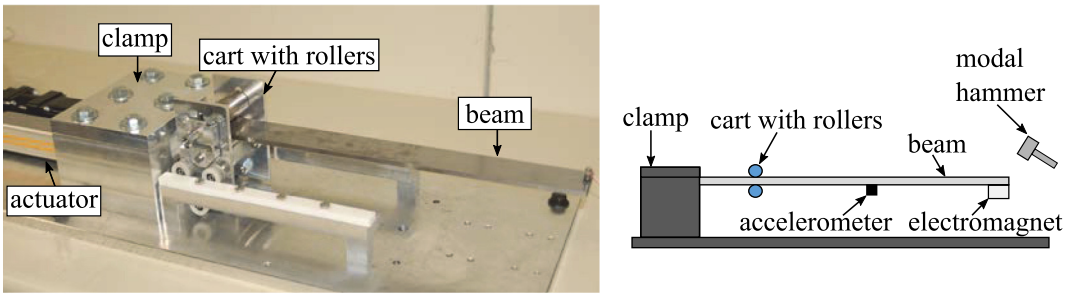

Fig. 1. (a) Picture; and (b) schematic of the DROPBEAR testbed.

$$\hat{\mathbf{q}}_p(t) = \left(\mathbf{\Phi}_{mp}^{\mathrm{T}}\mathbf{\Phi}_{mp}\right)^{-1}\mathbf{y}_p(t) \tag{6}$$

yielding

$$\hat{\mathbf{q}}_p(t) = \mathbf{\Phi}_{mp}^{+}\mathbf{x}_m(t) = \left(\mathbf{\Phi}_{mp}^{\mathrm{T}}\mathbf{\Phi}_{mp}\right)^{-1}\mathbf{\Phi}_{mp}^{\mathrm{T}}\mathbf{x}_m(t) \quad (m > p) \tag{7}$$

where $\mathbf{\Phi}_{mp}^{+}$ is the pseudo inverse of matrix $\mathbf{\Phi}_{mp}$. Alternatively, Eq. (7) can be obtained using a least squares estimation of $\mathbf{x}_m(t)$ from $\mathbf{\Phi}_{mp}\hat{\mathbf{q}}_p(t)$.

Substituting Eq. (6) into Eq. (3), the coordinate transformation matrix is obtained:

$$\mathbf{T} = \mathbf{\Phi}_p\mathbf{\Phi}_{mp}^{+\,\mathrm{T}} = \begin{bmatrix} \mathbf{\Phi}_{mp}\mathbf{\Phi}_{mp}^{+} \\ \mathbf{\Phi}_{sp}\mathbf{\Phi}_{sp}^{+} \end{bmatrix} \tag{8}$$

The DOFs of the full order can be reduced in the form:

$$\mathbf{x}(t) = \begin{bmatrix} \mathbf{x}_m(t) \\ \mathbf{x}_s(t) \end{bmatrix} = \mathbf{T}\mathbf{x}_m(t) \tag{9}$$

Using the coordinate transformation matrix $\mathbf{T}$, and reducing the system matrix to a single DOF ($m = 1$), the system matrices in Eq. 1 has the form:

$$m\ddot{x}(t) + c\dot{x}(t) + kx(t) = r(t) \tag{10}$$

with:

$$k = \mathbf{T}^{\mathrm{T}}\mathbf{K}\mathbf{T} = \mathbf{\Phi}_{mp}^{+\,\mathrm{T}}\mathbf{\Lambda}_{pp}\mathbf{\Phi}_{mp}^{+}, m = \mathbf{T}^{\mathrm{T}}\mathbf{M}\mathbf{T} = \mathbf{\Phi}_{mp}^{+\,\mathrm{T}}\mathbf{\Phi}_{mp}^{+}, c = \mathbf{T}^{\mathrm{T}}\mathbf{C}\mathbf{T} = \alpha\mathbf{\Phi}_{mp}^{+\,\mathrm{T}}\mathbf{\Lambda}_{pp}\mathbf{\Phi}_{mp}^{+}, r = \mathbf{T}^{\mathrm{T}}\mathbf{r} = \mathbf{\Phi}_{mp}^{+\,\mathrm{T}}\mathbf{\Phi}_p\mathbf{r} \tag{11}$$

where $\mathbf{\Lambda}_{pp}$ is the eigenvalue matrix containing the first p eigenvalues, and damping matrix $\mathbf{C}$ is proportional to $\mathbf{K}$.

In this paper, the FEM of DROPBEAR is used to create a simplified representation by means of SEREP, with an number of DOFs equal to the number of sensors, here yielding an SDOF representation.

2.3. Problem formulation

The reduced order dynamic system can be written:

$$\dot{\mathbf{x}} = f(\mathbf{x}, r) = f^0(\mathbf{x}, \mathbf{r}) + g(\mathbf{x}, \mathbf{r}) \tag{12}$$

where $\mathbf{x} = [x_1, x_2, \ldots, x_{2m}]^{\mathrm{T}} \in \mathbb{R}^{2m\times 1}$ is the state vector, $\mathbf{r} = [r_1, r_2, \ldots, r_n]^{\mathrm{T}} \in \mathbb{R}^{n\times 1}$ is the input vector, $f : \mathbb{R}^{2m\times 1} \times \mathbb{R}^{n\times 1} \to \mathbb{R}^{2m\times 1}$is a function describing the dynamics with $f^0 : \mathbb{R}^{2m\times 1} \times \mathbb{R}^{n\times 1} \to \mathbb{R}^{2m\times 1}$denoting the known dynamics and $g : \mathbb{R}^{2m\times 1} \times \mathbb{R}^{n\times 1} \to \mathbb{R}^{2m\times 1}$ the unknown dynamics.

The state estimation problem becomes the estimation of the unknown function g. This can be done by linearizing the function using a basis function $\sigma(\mathbf{x}, \mathbf{r})$ and lumping the unknown parameters in a matrix $\boldsymbol{\theta}$ that is convenient to the parameter estimation task:

$$g(\mathbf{x}, \mathbf{r}) = \boldsymbol{\theta}^{\mathrm{T}}\sigma(\mathbf{x}, \mathbf{r}) \tag{13}$$

where $\sigma : \mathbb{R}^{2m\times 1} \times \mathbb{R}^{n\times 1} \to \mathbb{R}^{P\times 1}$, P denotes the number of basis functions, and $\boldsymbol{\theta} \in \mathbb{R}^{P\times 2m}$.

An adaptive model is constructed based on the knowledge of f^0, and function g is adaptively estimated using:

$$\hat{g}(\mathbf{x}, \mathbf{r}) = \hat{\boldsymbol{\theta}}^{\mathrm{T}}\sigma(\mathbf{x}, \mathbf{r}) \tag{14}$$

where the hat denotes an estimation. The estimation error $\tilde{g}(\mathbf{x}, \mathbf{r})$ is formulated:

$$\tilde{g}(\mathbf{x}, \mathbf{r}) = g(\mathbf{x}, \mathbf{r}) - \hat{g}(\mathbf{x}, \mathbf{r}) = \left(\boldsymbol{\theta} - \hat{\boldsymbol{\theta}}\right)^{\mathrm{T}}\sigma(\mathbf{x}, \mathbf{r}) = \tilde{\boldsymbol{\theta}}^{\mathrm{T}}\sigma(\mathbf{x}, \mathbf{r}) \tag{15}$$

It follows that an adaptive algorithm needs to be designed such that $\hat{\boldsymbol{\theta}}(t) \to \boldsymbol{\theta}(t)$ for $t \to \infty$. However, this convergence can only be guaranteed if and only if the vector signal $\boldsymbol{\sigma}$ is persistently exciting [25]. A signal $\boldsymbol{\sigma} \in \mathbb{R}^{2m\times 1}$ is persistently exciting at a level ρ_0 if it satisfies

$$\mathbf{S}_p = \int_t^{t+T_0} \sigma(t)\sigma^{\mathrm{T}}(t)\mathrm{d}t \geqslant \rho_0\mathbf{I} \tag{16}$$

for some $\rho_0 > 0, T_0 > 0$ and $\forall t \geqslant 0$, where $\mathbf{I}$ denotes the identity matrix. The signal is termed persistently exciting of order p if matrix $\mathbf{S}_p \in \mathbb{R}^{p\times p}$ is positive definite over any finite interval. A force applied over a short period of time, like that, typically experienced by high rate systems, is non-persistent because of $\mathbf{S}_p \to 0\,\forall p$. The algorithm proposed in this research is

designed to provide an accurate estimate of $\hat{g}$ by relaxing the restrictive condition on the persistence of the excitation, based on CL.

3. Online parameter estimation algorithm

The adaptive algorithm for online parameter estimation is diagrammed in Fig. 2. The reference model consists of the reduced-order physical representation of DROPBEAR, written in the state-space format:

$$\dot{\mathbf{z}} = \mathbf{A}\mathbf{z} + \mathbf{b}g(\mathbf{z}, r) \tag{17}$$

where $\mathbf{z} \in \mathbb{R}^{2m\times 1}$ is the state vector, $\mathbf{A} \in \mathbb{R}^{2m\times 2m}$ is the state-space matrix, $\mathbf{b} \in \mathbb{R}^{2m\times 1}$ is the input position vector, and $g(\mathbf{z}, r)$ is the input, with:

$$\mathbf{A} = \begin{bmatrix} \mathbf{0}_{2m-1\times 1} & \mathbf{I}_{2m-1\times 2m-1} \\ & \mathbf{0}^{\mathrm{T}}_{2m\times 1} \end{bmatrix}, \quad \mathbf{b} = \begin{bmatrix} \mathbf{0}_{2m-1\times 1} \\ 1 \end{bmatrix} \tag{18}$$

The formulation of the adaptive model starts using:

$$\dot{\hat{\mathbf{z}}} = \mathbf{A}\hat{\mathbf{z}} + \mathbf{b}\hat{g}(\mathbf{z}, r) \tag{19}$$

along with the estimation law for g proposed by [21]:

$$g(\mathbf{z}, r) \approx 2\dot{z}_m + \mathbf{L}^{\mathrm{T}}(\mathbf{z} - \hat{\mathbf{z}}) - \hat{g}(\mathbf{z}, r) \tag{20}$$

giving:

$$\dot{\hat{\mathbf{z}}} = \mathbf{A}\hat{\mathbf{z}} + \mathbf{b}\Big(2\dot{z}_{2m} + \mathbf{L}^{\mathrm{T}}(\mathbf{z} - \hat{\mathbf{z}}) - \hat{g}(\mathbf{z}, r)\Big) \tag{21}$$

where $\dot{z}_{2m} = g(\mathbf{z}, r)$ is the state's time derivative of the $2m$-th measurement, and $\mathbf{L}^{\mathrm{T}} = [L_1, L_2, \ldots, L_{2m}]^{\mathrm{T}} \in \mathbb{R}^{2m\times 1}$ is an observer gain vector with positive elements.

Consider the tracking error $\tilde{\mathbf{z}} = \hat{\mathbf{z}} - \mathbf{z}$. Expanding Eq. (21) yields

$$\begin{bmatrix} \dot{\hat{\mathbf{z}}}_{2m-1} \\ \dot{\hat{z}}_{2m} \end{bmatrix} - \dot{z}_{2m} = \begin{bmatrix} 0 & 1 \\ 0 & 0 \end{bmatrix} \begin{bmatrix} \hat{\mathbf{z}}_{2m-1} \\ \hat{z}_{2m} \end{bmatrix} + \begin{bmatrix} 0 \\ 1 \end{bmatrix} \Big(g(\mathbf{z}, r) + \mathbf{L}^{\mathrm{T}}(\mathbf{z} - \hat{\mathbf{z}}) - \hat{g}(\mathbf{z}, r)\Big) \tag{22}$$

Extracting the last row of Eq. (22), and considering the parameter estimation error in Eq. (14) yields:

$$\dot{\tilde{z}}_{2m} = -\mathbf{L}^{\mathrm{T}}\tilde{\mathbf{z}} + \tilde{g}(\mathbf{z}, r) \tag{23}$$

Lastly, substituting Eq. (23) back into Eq. (22), the error dynamics becomes:

$$\dot{\tilde{\mathbf{z}}} = \mathbf{A}\tilde{\mathbf{z}} + \mathbf{b}\Big(-\mathbf{L}^{\mathrm{T}}\tilde{\mathbf{z}} + \tilde{g}(\mathbf{z}, r)\Big) = \mathbf{A}_L\tilde{\mathbf{z}} + \mathbf{b}\tilde{g}(\mathbf{z}, r) \tag{24}$$

where $\mathbf{A}_L = \mathbf{A} - \mathbf{b}\mathbf{L}^{\mathrm{T}}$ is a Hurwitz matrix, for which all eigenvalues have strictly negative real parts, yielding a tracking error $\tilde{\mathbf{z}}$ that converges to zero exponentially if $\dot{z}_{2m} - \hat{g}(\mathbf{z}, r) = 0$ and $\mathbf{z} - \hat{\mathbf{z}} = \mathbf{0}$ [26]. It follows from Lyapunov theory that there always exists a unique positive definite matrix $\mathbf{P} \in \mathbb{R}^{2m\times 2m}$ for any positive-definite symmetric matrix $\mathbf{Q} \in \mathbb{R}^{2m\times 2m}$ for $\mathbf{A}_L$ stable:

$$\mathbf{A}_L^{\mathrm{T}}\mathbf{P} + \mathbf{P}\mathbf{A}_L + \mathbf{Q} = 0 \tag{25}$$

3.1. Adaptation law

Take the following adaptive law that uses instantaneous data for updating the estimates:

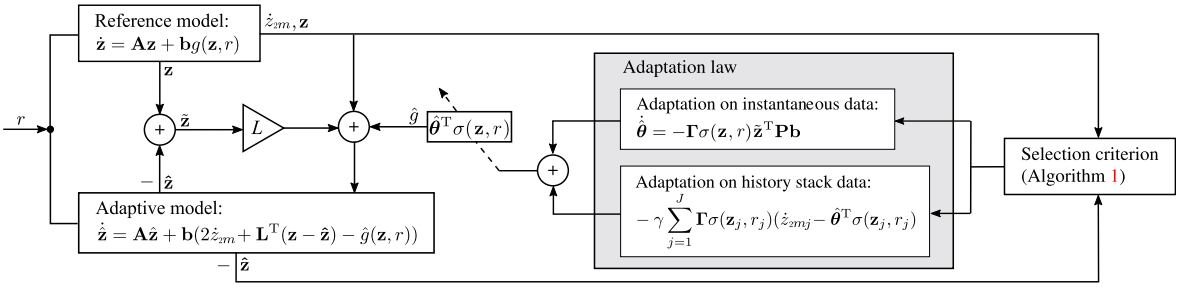

Fig. 2. Block diagram of the online parameter estimation algorithm.

$$\dot{\hat{\theta}} = -\mathbf{\Gamma}\sigma(\mathbf{z},\mathbf{r})\tilde{\mathbf{z}}^{\mathrm{T}}\mathbf{P}\mathbf{b} \tag{26}$$

where $\mathbf{\Gamma}$ is a diagonal learning rate matrix constructed of positive definite elements, and basis function $\sigma(\mathbf{z},\mathbf{r}) \in \mathbb{R}^{p\times 1}$ is the vector defined in Eq. 12 and consists of reduced system parameters k, m, c, and r. To relax the requirement on the persistence of the excitation based on CL [26], a history stack $\mathscr{H} = \sum_{j=1}^{J}\sigma(\mathbf{z},r)\sigma(\mathbf{z},r)^{\mathrm{T}}$ containing a finite number of past input–output data is combined with instantaneous data points to update the estimate $\hat{\theta}$. Eq. 27 is augmented with the state derivative estimation error $e_j = \dot{z}_{2mj} - \hat{\theta}^{\mathrm{T}}\sigma(\mathbf{z}_j,\mathbf{r}_j)$ for data points $j = 1,2,\ldots,\bar{J}$:

$$\dot{\hat{\theta}} = -\mathbf{\Gamma}\sigma(\mathbf{z},r)\tilde{\mathbf{z}}^{\mathrm{T}}\mathbf{P}\mathbf{b} - \gamma\sum_{j=1}^{J}\mathbf{\Gamma}\sigma(\mathbf{z}_j,r_j)\left(\dot{z}_{2mj} - \hat{\theta}^{\mathrm{T}}\sigma(\mathbf{z}_j,r_j)\right) = -\mathbf{\Gamma}\sigma(\mathbf{z},r)\tilde{\mathbf{z}}^{\mathrm{T}}\mathbf{P}\mathbf{b} - \gamma\sum_{j=1}^{J}\mathbf{\Gamma}\sigma(\mathbf{z}_j,r_j)e_j \tag{27}$$

where $\gamma > 0$ is a constant learning gain used to adjust the contribution of past error $\mathbf{e}$. The adaptation law in Eq. (26) drives the parameter estimation to a ball around the origin without a persistent excitation if $\mathscr{H}$ is sufficiently rich, where $\mathscr{H}$ must contain a number of basis larger than that for σ. The size of the ball around the origin follows the order of e_j. If large derivative estimation errors are contained in $\mathscr{H}$, the parameter estimation will converge to a large error, in particular during the transient phase [27]. The convergence error be reduced by removing inaccurate data points, here done using the singular value maximizing algorithm developed by [28] and shown in Algorithm 1.

The singular value of matrix $\mathscr{H}$ is incremented with the arrival of new data points selected by Algorithm 1. In real-time implementations, the size of $\mathscr{H}$ is limited by a given threshold of $\bar{J}$ due to convergence rate considerations. The convergence rate is dependent on the spectral properties of $\mathscr{H}$, and directly proportional to the minimum singular value of the history stack matrix $\lambda_{\min}(\mathscr{H})$ where λ denotes a singular value. Matrix $\mathscr{H}$ is full rank only if $\mathrm{rank}(\mathscr{H}) = \bar{J}$. The objective of updating the history stack using Algorithm 1 is to feed in new data points into empty slots or to replace an existing slot with an increase in the instantaneous minimum singular value of $\mathscr{H}$. It follows that the estimation is Eq. (22) is guaranteed to perform better than that using the older data set, therefore resulting in a lower steady-state parameter estimation error.

Algorithm 1. Singular value maximizing algorithm for selecting data points in history stack.

if $\frac{\|\sigma(\mathbf{z}(t),r(t))-\sigma(\mathbf{z}_p,r_p)\|}{\|\sigma(\mathbf{z}(t),r(t))\|} \leqslant e$ or $\mathrm{rank}[\mathscr{H},\sigma(\mathbf{z},r)] > \mathrm{rank}(\mathscr{H})$
  if $J < \bar{J}$ **then**
    $J = J + 1$
    $p = J$
    $\mathscr{H}(:,J) = \sigma(\mathbf{z}(t),r(t))$
    $\Delta(J) = \dot{z}_{2m}$
  else
    $\mathscr{H}_{\mathrm{old}} = \mathscr{H}$
    $\mathbf{S}_{\mathrm{old}} = \min(\mathrm{SVD}(\mathscr{H}))$
    $\mathscr{H} = \mathscr{H}_{\mathrm{old}}$
    for $j = 1$ to J **do**
      $\mathscr{H}(:,J) = \sigma(\mathbf{z}(t),r(t))$
      $S(j) = \min(\mathrm{SVD}(\mathscr{H}))$
      $\mathscr{H} = \mathscr{H}_{\mathrm{old}}$
    end for
    find $\mathbf{S}_{\max}$ and let p denote the corresponding column index.
    if $\mathbf{S}_{\max} > \mathbf{S}_{\mathrm{old}}$ **then**
      $\mathscr{H}(:,J) = \sigma(\mathbf{x}(t),r(t))$
      Store $\Delta(J) = \dot{z}_{2m}$
    end if
  end if
end if

3.2. Stability analysis

To show stability of the adaptation law, consider the following Lyapunov function V:

$$V(\xi) = \frac{1}{2}\tilde{\mathbf{z}}^{\mathrm{T}}\mathbf{P}\tilde{\mathbf{z}} + \frac{1}{2}\tilde{\theta}^{\mathrm{T}}\mathbf{\Gamma}^{-1}\tilde{\theta} \tag{28}$$

where $\xi = [\tilde{\mathbf{z}}, \tilde{\theta}]^{\mathrm{T}}$, with V positive definite and containing all time-varying parameters. Using the Raleigh-Ritz Theorem, the Lyapunov function V is bounded by:

$$\tfrac{1}{2}\min\left\{\lambda_{\min}(\mathbf{P}), \lambda_{\min}\left(\Gamma^{-1}\right)\right\}\|\xi\|^2 \leqslant V(\xi) \leqslant \tfrac{1}{2}\max\left\{\lambda_{\max}(\mathbf{P}), \lambda_{\max}\left(\Gamma^{-1}\right)\right\}\|\xi\|^2 \tag{29}$$

Taking the time derivative $\dot{V}$ and substituting Eqs. (25) and (27) yields:

$$\dot{V}(\xi) = -\frac{1}{2}\tilde{\mathbf{z}}^{\mathrm{T}}\mathbf{Q}\tilde{\mathbf{z}} + \tilde{\mathbf{z}}^{\mathrm{T}}\mathbf{P}\mathbf{b}\tilde{\theta}^{\mathrm{T}}\sigma(\mathbf{z}, r) + \tilde{\theta}^{\mathrm{T}}\left(-\sigma(\mathbf{z}, r)\tilde{\mathbf{z}}^{\mathrm{T}}\mathbf{P}\mathbf{b} - \gamma\sum_{j=1}^{J}\sigma(\mathbf{z}_j, r_j)\sigma\left(\mathbf{z}_j, r_j^{\mathrm{T}}\right)\hat{\theta}\right) = -\frac{1}{2}\tilde{\mathbf{z}}^{\mathrm{T}}\mathbf{Q}\tilde{\mathbf{z}} - \tilde{\theta}^{\mathrm{T}}\sigma(\mathbf{z}_j, r_j)\sigma(\mathbf{z}_j, r_j)^{\mathrm{T}}\tilde{\theta} \tag{30}$$

The derivative of Eq. (30) satisfies the following inequality:

$$\dot{V}(\xi) \leqslant -\frac{1}{2}\lambda_{\min}(\mathbf{Q})\|\tilde{\mathbf{z}}\|^2 - \lambda_{\min}(\Omega)\|\tilde{\theta}\|^2 \leqslant -\frac{1}{2}\min\{\lambda_{\min}(\mathbf{Q}), 2\lambda_{\min}(\mathbf{\Omega})\}\|\tilde{\xi}\|^2 \tag{31}$$

Eq. (31) shows that $\dot{V}$ is negative outside of the compact set $-\frac{1}{2}\min\{\lambda_{\min}(\mathbf{Q}), 2\lambda_{\min}(\mathbf{\Omega})\}\|\tilde{\xi}\|^2$. Combining the bounded error of V in Eq. (30), $\dot{V}$ can be reduced to:

$$\dot{V}(\xi) \leqslant -\frac{\min\{\lambda_{\min}(\mathbf{Q}), 2\lambda_{\min}(\mathbf{\Omega})\}}{\max\{\lambda_{\max}(\mathbf{Q}), \lambda_{\max}(\mathbf{\Gamma}^{-1})\}}V(\xi) \tag{32}$$

In Eq. (32), $\lambda_{\min}(\mathbf{\Omega})$ is guaranteed to be monotonically increasing through the singular value maximization (Algorithm 1), and matrices $\mathbf{Q}$ and $\mathbf{P}$ are positive definite matrix. Hence, $\dot{V}$ is guaranteed to be negative, and exponentially stability is established, with $\hat{\theta} \to \theta$.

4. Numerical validation

The proposed algorithm is first validated through numerical simulations by assessing the performance of the CL algorithm at conducting high-rate state estimation. The example model consists of an SDOF mass-spring-damper system of dynamics:

$$\begin{bmatrix}\dot{z}_1\\ \dot{z}_2\end{bmatrix} = \begin{bmatrix}0 & 1\\ 0 & 0\end{bmatrix}\begin{bmatrix}z_1\\ z_2\end{bmatrix} + \begin{bmatrix}0\\ 1\end{bmatrix}g(\mathbf{z}, r) \tag{33}$$

with

$$g(\mathbf{z}, r) = \theta^{\mathrm{T}}\sigma(\mathbf{z}, r) = [\theta_1\theta_2 1]\left[-\frac{k}{m}z_1 - \frac{c}{m}z_2\frac{r}{m}\right]^{\mathrm{T}} \tag{34}$$

Simulations are conducted for one and two uncertain parameters, all ran over 1 s using a synthetic sampling rate of 25,600 Hz. The one uncertain parameter consists of an uncertain stiffness mimicking an uncertain boundary condition, while the two uncertain parameters consists of both a varying mass and stiffness mimicking DROPBEAR's drop in mass and change in cart position.

4.1. One uncertain parameter

For the single uncertain parameter simulations, it is assumed that parameters c and k are known, and the external excitation r is taken as unmeasurable, treated as an unmodeled disturbance whereas the system is assumed under free vibration. The single uncertain parameter k is implicitly contained in θ_1 that pre-multiplies k/m. It follows that the reference model is given by

$$g(\mathbf{z}, r) = \theta^{\mathrm{T}}\sigma(\mathbf{z}, r) = [\theta_1 1]\left[-\frac{k}{m}z_1 - \frac{c}{m}z_2\right]^{\mathrm{T}} \tag{35}$$

with known parameters $m = 1$ kg and $c = 1$ Ns/m, assumed uncertain parameter $k = 500$ N/m, and unknown parameter $\theta_1 = 0.8$. The system is excited by the impulse signal $r(t)$ with an amplitude of 100 g_n at 50 ms plotted in Fig. 3. The initial conditions are set to $\mathbf{z} = [0 \quad 0]^{\mathrm{T}}$ and $\theta_1 = 0$. The observer gain is taken as $\mathbf{L} = [500 \quad 1]^{\mathrm{T}}$, and learning rates $\Gamma = 100$ and $\gamma = 0.5$. The history stack includes $\bar{J} = 30$ input-out data sets, where the oldest data point is constantly replaced by the newest data point selected based on Algorithm 1. The positive-definite symmetric $\mathbf{Q}$ matrix is taken as $\mathbf{Q} = \mathbf{I}$.

The tracking performance of the states are shown in Fig. 4 with and without the CL adaptation rule. Results show that the adaptive algorithm is successful at tracking the states and identifying the uncertain parameter when CL is integrated with the adaptation law, and that ignoring the CL component does not yield accurate information on the system due to erroneous instantaneous data feedback during the transient phase. Under CL, the estimated θ_1 approaches the real value $\theta_1 = 0.8$, 59 ms after the impulse (Fig. 5(a)). Note that the parameter estimation errors stay exponentially bounded within a neighborhood of the reference values, and here the estimation is said to have converged when it falls and remains within a 5% error threshold.

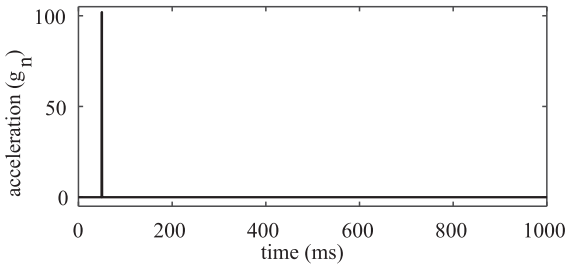

Fig. 3. External excitation to the system, one uncertain parameter case.

Fig. 5(b) shows the evolution of the minimum singular value selected in the history stack for the updating. The plot shows that increasing the singular value using Algorithm 1 provides a fast and accurate convergence.

4.2. Two uncertain parameters

Simulations above are repeated, but this time is taking two uncertain parameters: k and m. Function g is modified to

$$g(\mathbf{z}, r) = \boldsymbol{\theta}^{\mathrm{T}}\sigma(\mathbf{z}, r) = [\theta_1 \theta_2]\left[-\frac{k}{m}z_1 - \frac{c}{m}z_2\right]^{\mathrm{T}} \tag{36}$$

The stiffness of the system starts with $k = 750$ N/m, and reduces to $k = 500$ N/m at 300 ms. The mass starts at $k = 1$ kg and reduces to $k = 0.5$ kg at 300 ms. Damping $c = 1$ Ns/m is kept constant through the simulations. The external excitation, plotted in Fig. 6 has an impulse of 100 g_n applied at 50 ms, an impulse of 150 g_n amplitude applied at 300 ms that coincides with the changes in the system parameters, and an impulse of 150 g_n amplitude applied at 600 ms, that is, 50 ms after the second set of changes in the system parameters. Values for k and m are initialized at k = 500 N/m and m = 1 kg, yielding θ_1 = 1.5 and θ_2 = 1 before $t = 300$ ms, and θ_1 = 2 and θ_2 = 2 thereafter. These values are set back to their initial values at 550 ms.

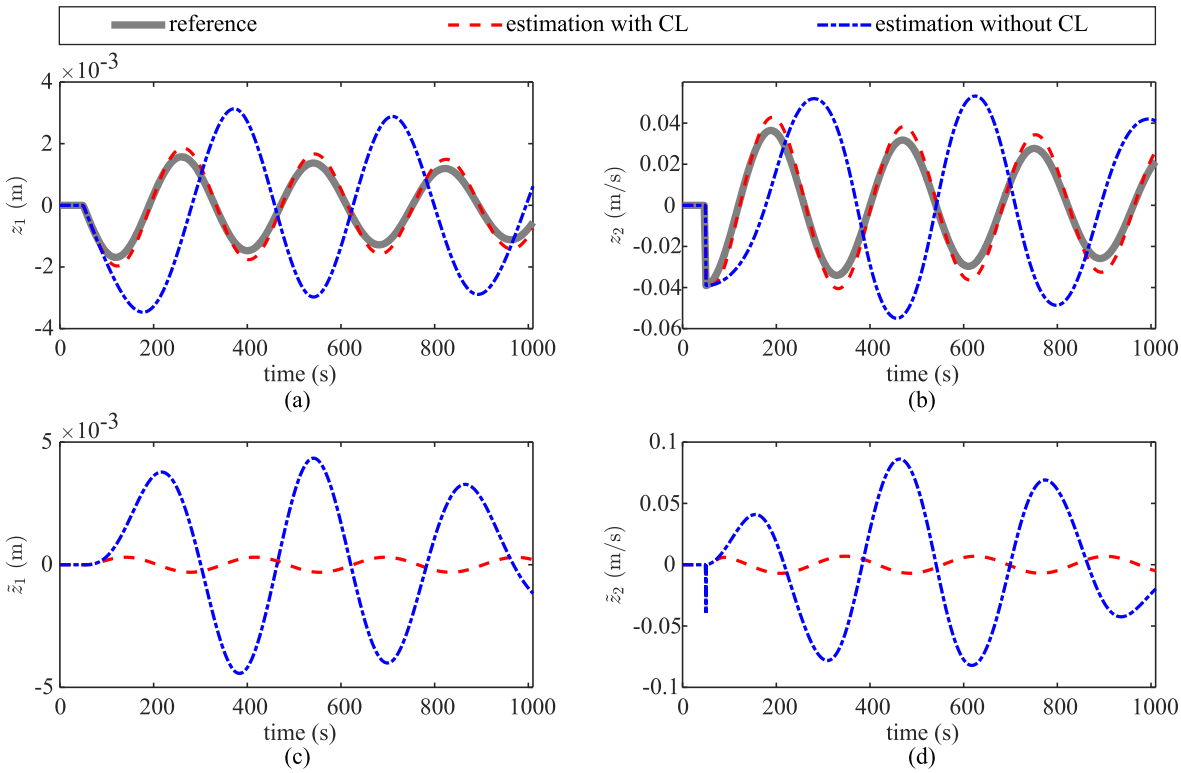

Fig. 4. Real versus estimated states with and without CL for one uncertain parameter: (a) tracking performance for z_1; (b) tracking performance for z_2; (c) tracking error $\tilde{z}_1$; and (d) tracking error $\tilde{z}_2$.

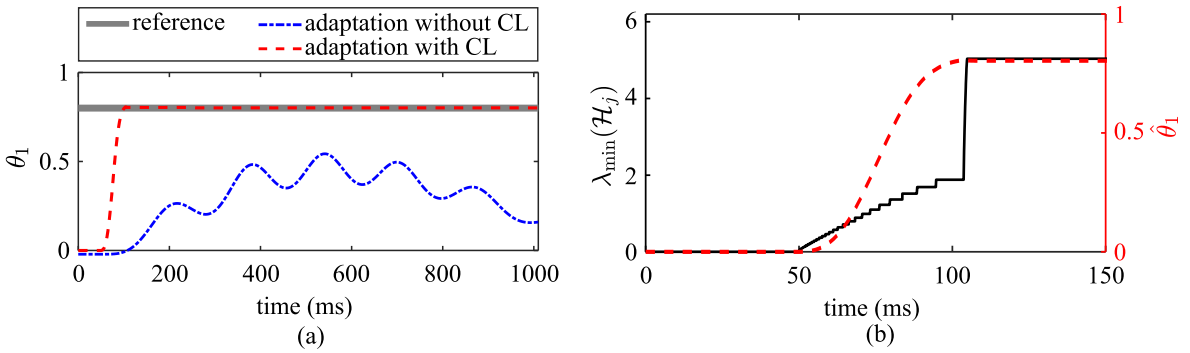

Fig. 5. Simulation results for one uncertain parameter: (a) evolution of parameter θ_1 with and without CL; and (b) evolution of the minimum singular value of the history stack versus θ_1 with CL for the first 150 ms.

The observer gain is set to $\mathbf{L} = [\,100 \quad 5\,]^{\mathrm{T}}$, and learning rates to $\mathbf{\Gamma} = [\,1\mathrm{e}2 \quad 0; \quad 0 \quad 1\mathrm{e}4\,]$ and $\gamma = 0.5$.Fig. 7 plots the time series results for state estimation with and without the CL adaptation rule and the associated tracking errors. CL is exhibiting good convergence and tracking of both states. Fig. 8(a) shows the parameter identification results along with the variation in the minimum singular value (Fig. 8(c)). The solid dashed red and dashed-dotted blue lines represent the real and estimated parameters of θ_1 and θ_2, respectively. The parameter identification results without CL is unsatisfactory as shown in 7 due to large state estimation errors (Fig. 8(b)). In contrast, after the initial impulse is applied to the system, the estimation with CL overshoots and exponentially converged to θ_1 after approximately 65 ms, and to θ_2 after approximately 85 ms. After the change in mass at $t = 300$ ms, the estimated parameters rapidly converge to the correct values θ_1 and θ_2, with a convergence time of 138 ms and 82 ms after the second impulse, respectively. After θ_1 and θ_2 are back to their initial values at 550 ms, the tracking error deviates until the impulse at 600 ms is applied, after which overshoots are observed before the estimations converge. The parameter θ_1 took approximately 60 ms to converge after the third impulse, and θ_2 took approximately 129 ms to converge after the third impulse.

5. Experimental validation

After the numerical verification, the proposed algorithm is experimentally validated on the DROPBEAR testbed. A first set of data sampled at 25,600 Hz was generated for various static cart positions and is examined in what follows. Another set of data sampled at 25,000 Hz was generated by moving the cart back-and-forth along the beam to produce a time-varying example, and will be examined in the subsequent section. Displacement and velocity measurements were obtained through the integration of the acceleration using the Newmark-beta method. Data was pre-filtered using a low pass filter to improve integration stability.

5.1. Static cart experiments

Static cart positions were produced by placing the rollers at 50 mm, 100 mm, 150 mm, and 200 mm from the clamp, while maintaining the mass at the tip. Data from the accelerometer was used for the estimation. Tests, listed in Table 1, were repeated five times under each configuration. A modal hammer was used to hit the beam at its tip at t = 250 ms. Fig. 9 plots the frequency response functions (FRFs) computed from experimental data, and resulting values for the fundamental frequencies listed in Table 1.

With the reduced SDOF representation, it is assumed that the change in position of the cart alters the stiffness and damping of the beam, and both k and c are taken as the uncertain parameters with the input force from the impact hammer taken as unmeasurable:

$$g(\mathbf{z}, r) = \boldsymbol{\theta}^{\mathrm{T}}\sigma(\mathbf{z}, r) = [\theta_1 \theta_2]\left[-\frac{k}{m}z_1 - \frac{c}{m}z_2\right]^{\mathrm{T}} \tag{37}$$

The initial conditions and values of the parameter vector are all set to null. Thus, before the first impact, there is no measurable response and the system's initial frequency is 0. The observer gain $\mathbf{L} = [\,1\mathrm{e}6 \quad 1\mathrm{e}3\,]^{\mathrm{T}}$, matrix $\mathbf{Q} = 1\mathrm{e}7\mathbf{I}$, learning rates $\mathbf{\Gamma} = [\,1 \quad 0; \quad 0 \quad 3\mathrm{e}4\,]$ and $\gamma = 1$, and history stack length $\bar{J} = 30$ (see Fig. 10).

Values obtained for θ_1 were used to compute the estimated fundamental frequency of the system. The evolution of the estimated frequencies are plotted in Fig. 9(a), where the gray line is the frequency obtained from the FRFs, the red dashed line is the estimation of the frequency, and the blue dashed line is the convergence point. From the figures, one can observed that all of the frequencies are tracked correctly. Table 1 summarizes the average estimated frequencies under each test group compared against the frequencies obtained from the FRFs, and the average convergence time. A comparison of the average

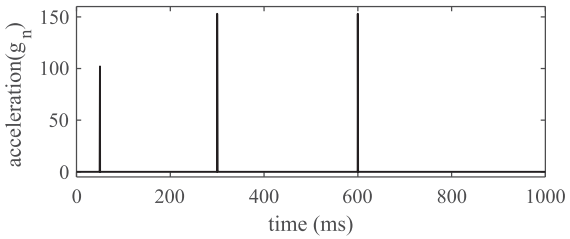

Fig. 6. External excitation to the system, two uncertain parameters case..

frequencies shows that the algorithm yields a very good estimation with a maximum error of 0.17% at the 50 mm position. While the system's damping is unknown, results in Fig. 9(b) show that the adaptive model converges to given damping values of adequate magnitude (see Fig. 11) through the estimation of θ_2. Fig. 11 is a graphical representation of the results, showing the average and variance of the values. The frequencies are well estimated with high precision, and the convergence time for both θ_1 and θ_2 decreases while the frequency of the beam increases.

5.2. Moving cart experiment

The last experiment, illustrated in Fig. 12, consists of locating the moving cart. Here, the cart starts at 50 mm from the clamp at 0.61 s, moves to 200 mm from the clamp over 1 s, stays for 1.39 s, and then returns to the initial position at 4.26 s, plotted in Fig. 13(a). During the experiment, the beam is struck by the impact hammer at 0.39 s, 2.17 s, 4.16 s, and 6.24 s with the amplitudes shown in Fig. 15(a).

A short-time fast Fourier transform using a moving Hanning window of 8192 data points is conducted in order to extract the temporal variation in frequency. Results are plotted in Fig. 13. The frequency of the beam varies between 21 Hz (initial cart position) and 37 Hz (farthest cart position).

Similar to the previous set of experiments, it is assumed that both k and c are uncertain, and the input force from the impact hammer taken as unmeasurable (Eq. (37)). The observer gain $\mathbf{L} = [\,1e5 \quad 1e3\,]^{\mathrm{T}}$, matrix $\mathbf{Q} = 1e8\mathbf{I}$, learning rates $\mathbf{\Gamma} = [\,1e1 \quad 0;\quad 0 \quad 3e4\,]$ and $\gamma = 1$, and history stack length $\bar{J} = 30$.

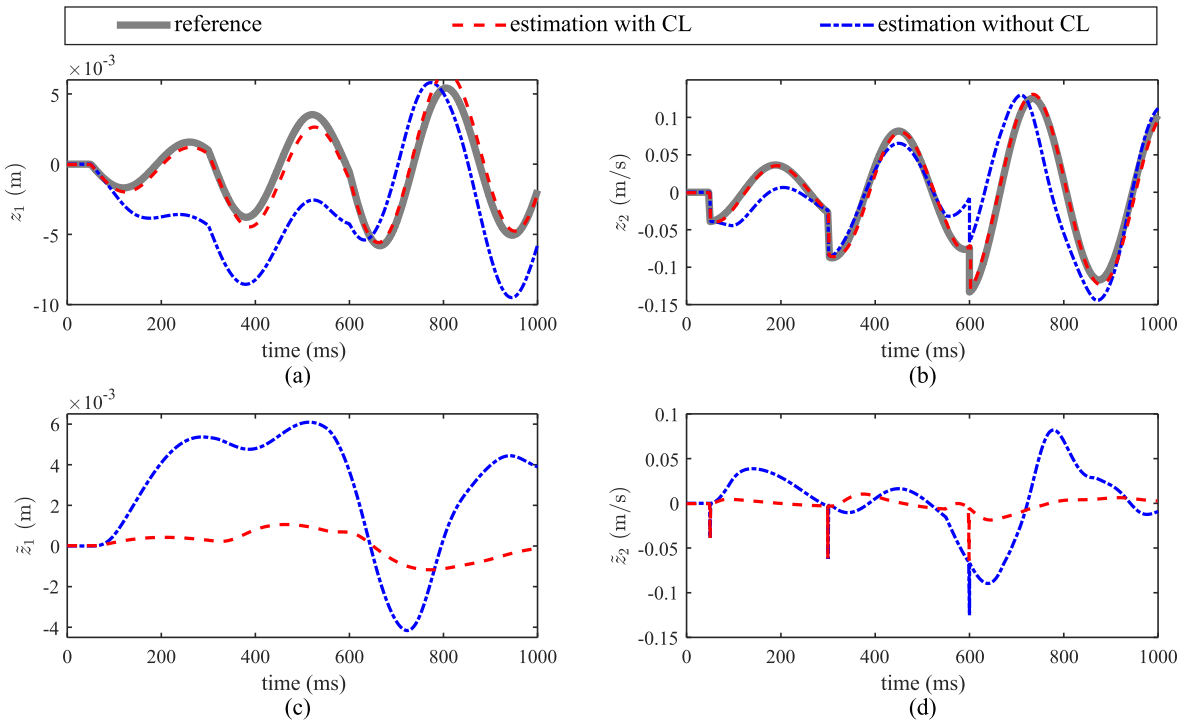

Fig. 7. Real versus estimated states with CL for two uncertain parameters: (a) tracking performance for z_1; (b) tracking performance for z_2; (c) tracking error $\tilde{z}_1$; and (d) tracking error $\tilde{z}_2$..

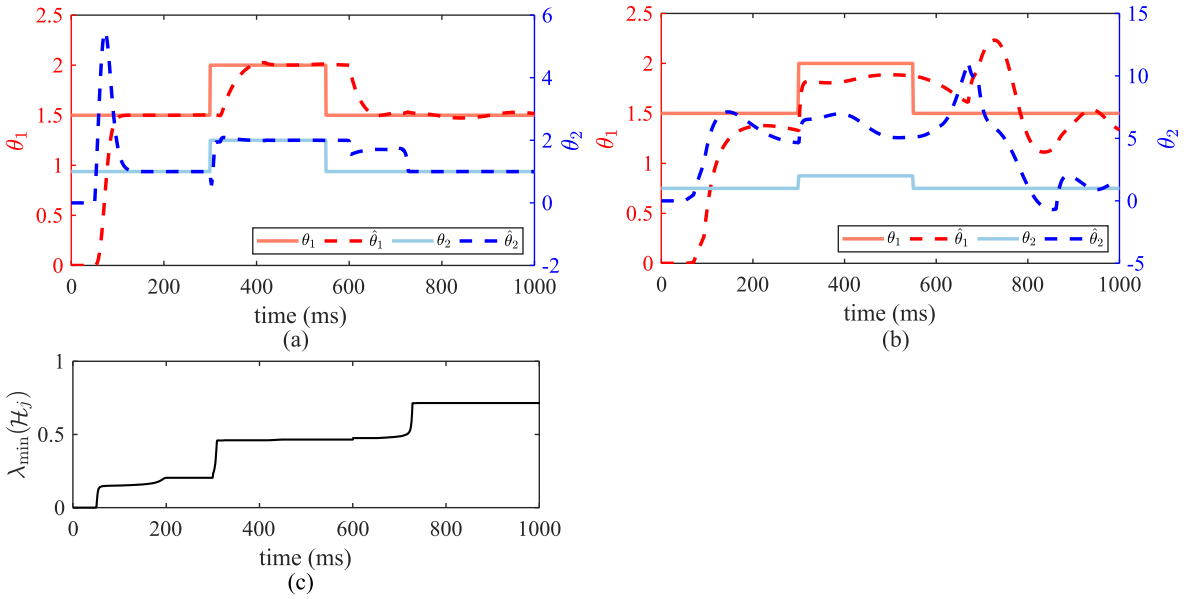

Fig. 8. Simulation results for two uncertain parameters: (a) evolution of parameters θ_1 and θ_2 with CL; (b) evolution of parameters θ_1 and θ_2 without CL; and (c) evolution of the minimum singular value of the history stack with CL.

Table 1
Comparison of first natural frequency extracted from the FRFs (frequency) and from the online parameter estimation algorithm (estimated frequency), and convergence time for the cart located at 50 mm, 100 mm, 150 mm, and 200 mm from the clamp.

Tests	Pin position	Frequency (Hz)	Estimated frequency (Hz)	Convergence time (ms)
1-5	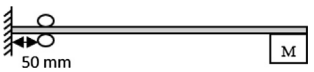	17.7	17.67	780
6-10		21.0	21.00	400
11-15		25.0	24.99	160
16-20	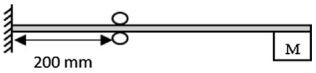	31.0	31.01	100

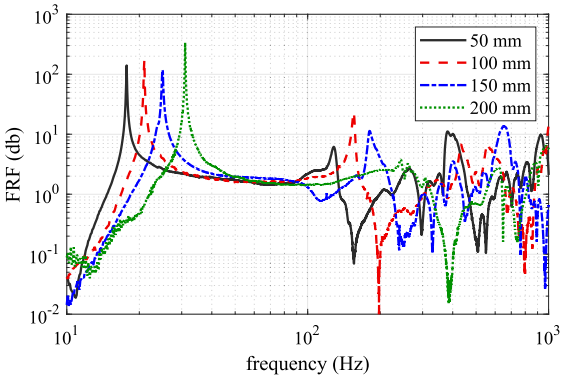

Fig. 9. Frequency response functions (FRFs) for the beam with mass under various cart position.

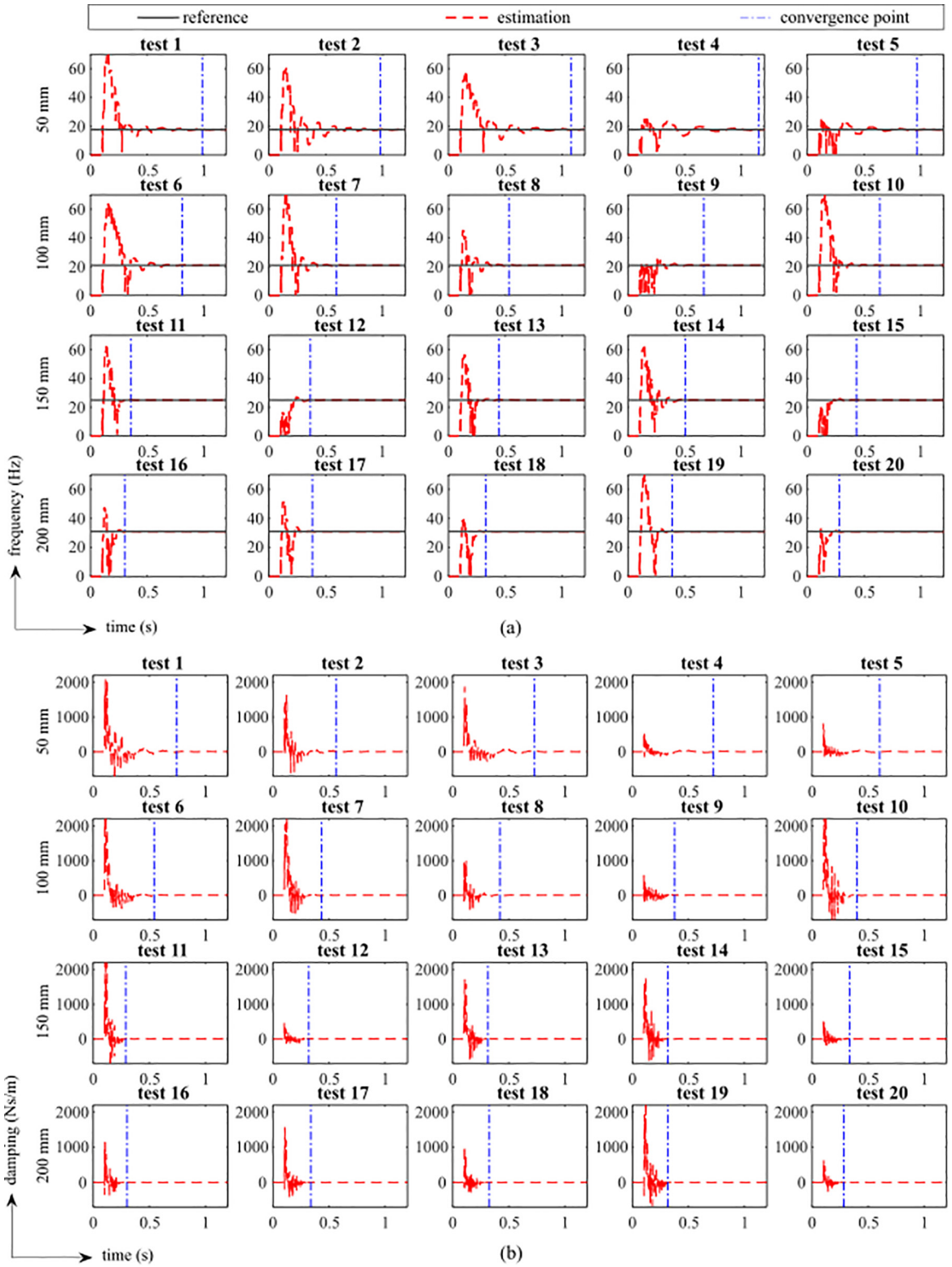

Fig. 10. Convergence of estimations for all tests: (a) frequency (from θ_1); and (b) damping (from θ_2).

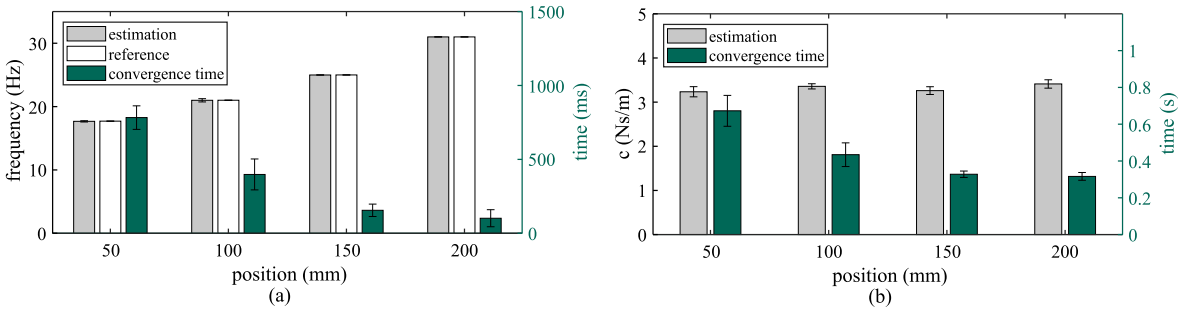

Fig. 11. Average and variance of the: (a) estimated frequency and convergence time under each cart position; and (b) estimated damping and convergence time under each cart position.

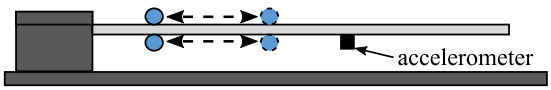

Fig. 12. Schematic of the moving cart experiment.

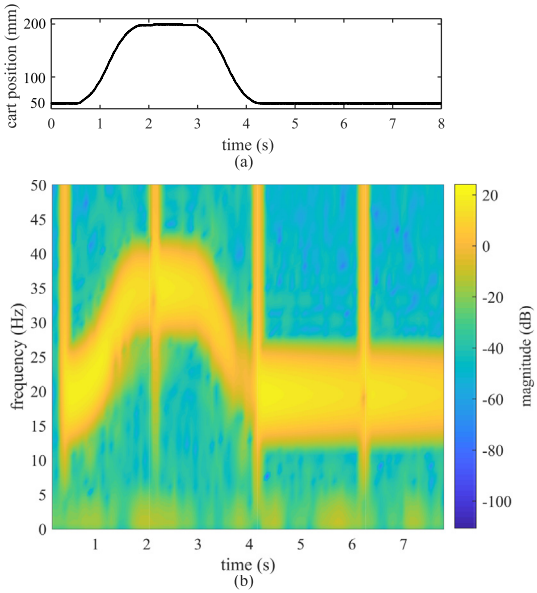

Fig. 13. (a) Time history of the moving cart position; and (b) results from the short-term fast Fourier transform.

The estimated states are plotted in Fig. 13 and compared with those from experimental measurements. The tracking errors are plotted in Figs. 14(c) and (d), exhibiting errors that are more apparent during the cart travel time and at impacts. An enlarged view of these tracking errors are plotted in Fig. 14(e) and (f).

Analogous to the previous subsection, it is assumed that there is a one-to-one map between the system's frequency and cart position. Note that the estimation of the map is out-of-the-scope of the paper but could easily be done through the finite element model or by investigating a prior set of experimental data. The estimation of θ_1 is converted to the estimated frequency, with results of the estimation plotted in Fig. 15(b) compared against the cart position. There is a good match between the estimated frequencies and cart positions, except during travel time where the algorithm exhibits some chattering and overshoots, yet with the travel zone closer to 200 mm being well estimated when the frequency of the system is higher, consistent with results from the static cart experiments. When the cart travels from 50 mm to 200 mm, an impact load is applied, and the estimation is chattering around the real values. The chattering can be reduced by setting the learning rates to smaller values, yet at the cost of the longer convergence time. When the cart moves back from 200 mm to 50 mm,

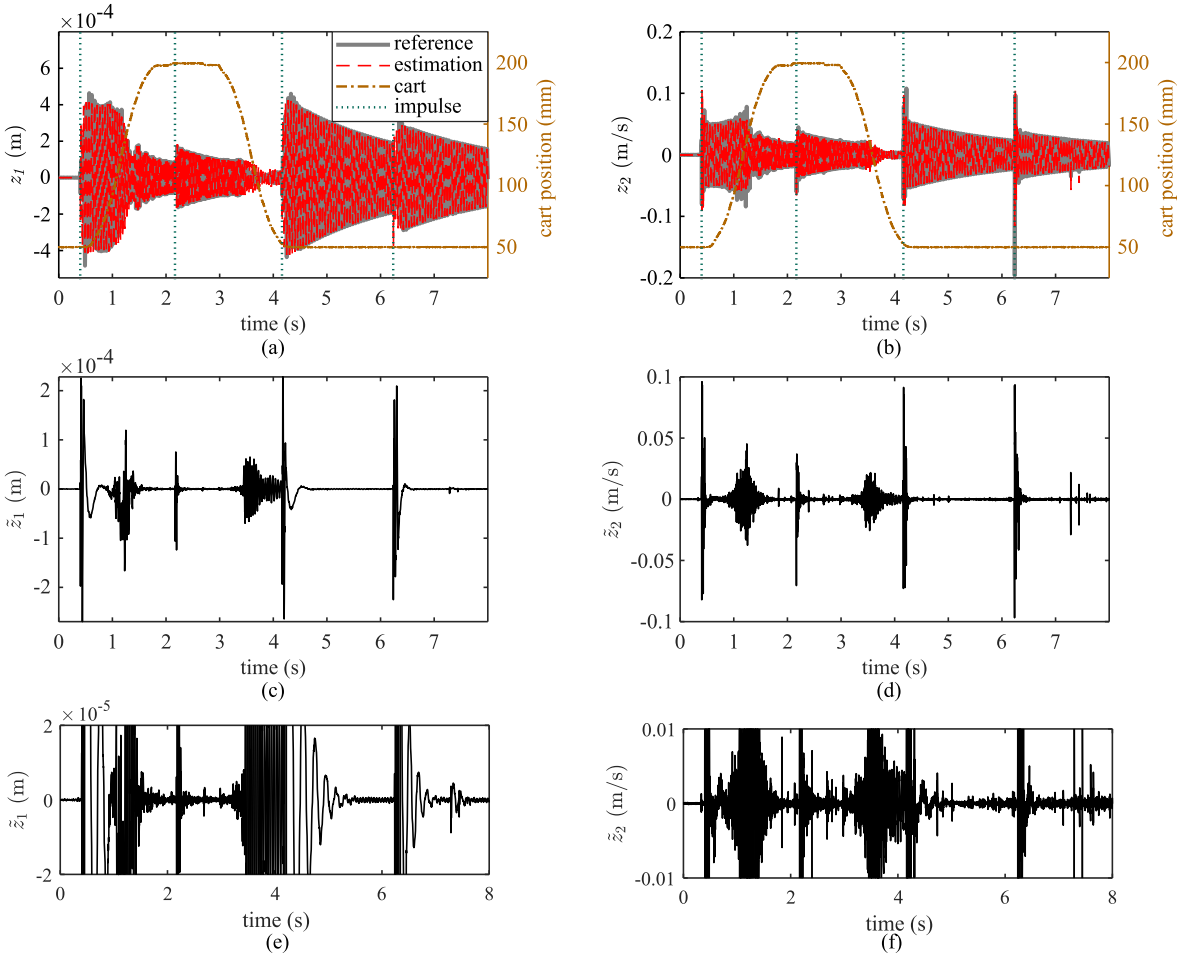

Fig. 14. Tracking performance results for moving cart experiment: (a) tracking performance for z_1; (b) tracking performance for z_2; (c) tracking error $\tilde{z}_1$; (d) tracking error $\tilde{z}_2$; (e) enlarged view of tracking error $\tilde{z}_1$; and (f) enlarged view of tracking error $\tilde{z}_2$..

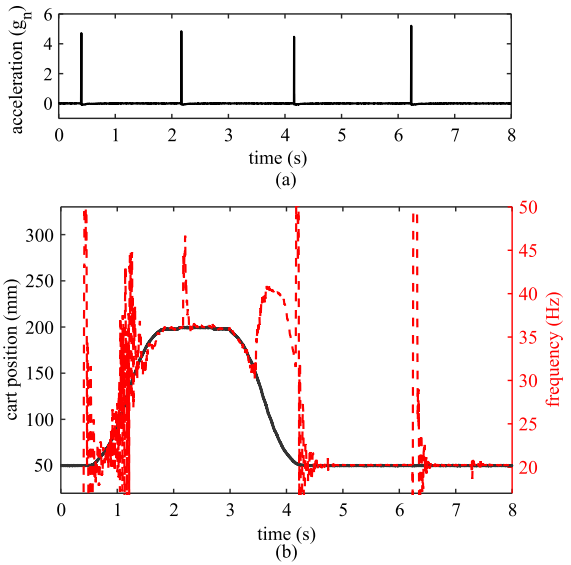

Fig. 15. (a) Time history plot of the impact force applied to the beam; and (b) estimated frequencies versus the cart positions.

the estimation starts to deviate about 47 ms after the cart initiates movement. A similar deviation is observed in the numerical simulation when parameter varies without synchronous impact. At the third impact at 4.16 s, the estimation rapidly converges back to the real value. The larger estimation error occurring during movement of the cart could be attributable to unmodeled dynamics having significant effects in the reduced order representation. This could be alleviated by the integration of nonlinear terms in the model. The larger errors during the travel time could also be attributed to the integration of acceleration measurements to obtain displacement and velocity states feeding in the algorithm. Alternative techniques include the use of other algorithms to improve the state estimates, as demonstrated by the authors in [29] using a neuro-estimator applied to high-rate systems and other types of sensors. This is left to future work.

5.3. Real-time applicability

Simulations of the algorithm were ran in MATLAB 2019a, with an Intel(R) Core(TM) i7-4770 CPU @ 3.40 GHz. Under that platform, the average computation time per sample is 93 μs with CL. The average computation time decreases to 87 μs with CL but without the singular value maximization, and 6 μs without the CL component. The computation time of the algorithm per sample compares well with the sampling rate of 25,000 Hz (samples were taken each 40 μs), although more than twice higher. It is envisioned, however, that the implementation of the algorithm on an FPGA along with refined coding will greatly reduce computation time, likely enabling applications above 25,600 Hz. Computation time can also be influenced by the history stack length, but so does the convergence time. Table 2 lists convergence time after the second, third, and fourth impact, for $\bar{J} = 10$, 30, and 50, along with the average computation time. These values compare well with results obtained from Downey et al. [15], where the authors reported an average convergence time of 202 ms and average computation time per step of 4.04 ms. Remark that these performance values were obtained experimentally, while work reported in this paper is conducted numerically. Results from Table 2 exhibit a clear trade-off between convergence time and computation time, whereas sub-millisecond capabilities in feedback are to be enabled on less accurate estimations. Acceptable performance on convergence time, linked to estimation accuracy, will be governed by the feedback application, while that on computation time by the desired sampling or application rate for real-time applicability.

6. Conclusion

This paper presented a time-based online parameter estimation algorithm for high-rate dynamics systems. The algorithm is based on a model reference adaptive system theory, where an adaptive model is constructed to reach a reference model or plant. The adaptive model consisted of a reduced order physical representation. The unknown parameters were represented linearly, and their adaptation was conducted based on the instantaneous error augmented with the error computed on a finite number of past events, a technique known as concurrent learning (CL). CL was leveraged to handle the lack of persistent excitation. Those past events were stored in a vector termed history stack, which vector was modified sequentially based on a singular value maximizing algorithm to accelerate convergence.

The proposed algorithm was first numerically verified on a single-degree-of-freedom model, investigating the capability of the algorithm to identify an uncertain stiffness (one uncertain parameter case), and to identify both a change in stiffness and a drop in mass after an impact (two uncertain parameters case). Under both cases, the algorithm exhibited great convergence properties. It was also demonstrated that the CL component was required to yield convergence to the correct value.

After, the algorithm was experimentally verified on the testbed DROPBEAR (Dynamic Reproduction of Projectiles in Ballistic Environments for Advanced Research), consisting of a cantilever beam with a moving cart that acted as a moving pin connection, defacto altering the beam's stiffness and damping. The beam was equipped with an accelerometer and excited with an impact hammer. Experimental data were generated for static cart locations and for a moving cart. The investigation also showed that the use of concurrent learning was critical in ensuring convergence when excitation persistence was not satisfied. Results from the static locations experimental tests showed that the algorithm was capable of correctly identifying the static cart locations with great accuracy and fast convergence time, where it was found that the convergence time substantially decreased with the increasing beam frequency. This relationship is also confirmed through the moving cart experiment, where results showed that the algorithm was capable of tracking the cart's position through the estimated frequency when impacts were applied. However, the estimate on the position exhibited chattering and overshoots during travel time that reduced when the beam frequency increased. The average computation speed of the algorithm per sample step,

Table 2
Comparison of convergence time after second, third, and fourth impulse under $\bar{J} = 10$, 30, and 50, along with average computation time per sample.

	Convergence time (ms)			Computation
$\bar{J}$	2nd impulse	3rd impulse	4th impulse	time/sample (μs)
10	161	432	327	64
30	144	289	264	95
50	131	249	136	112

implemented in MATLAB, was 93 μs. It is envisioned that the implementation of the algorithm on an FPGA along with refined coding will greatly reduce computation time, empowering real-time applications at high sampling rates.

It was hypothesized that the integration of acceleration measurements to obtain displacement and velocity states feeding in the algorithm could have been an important source of error in the estimation. It follows that further developments of the algorithm should include pure acceleration feedback strategies in order to improve the applicability to high-rate systems. In addition, the addition of nonlinear terms in the model could improve convergence by reducing the effects of unmodeled dynamics and other uncertainties. Overall, the results presented in this paper demonstrated the promise of the algorithm at high-rate state estimation, empowering field deployments of these systems through enhanced feedback capabilities.

Declaration of Competing Interest

The authors declare that they have no known competing financial interests or personal relationships that could have appeared to influence the work reported in this paper.

Acknowledgements

The work presented in this paper is partially funded by the Air Force Office of Scientific Research (AFOSR) under award number FA9550-17-1-0131, and the National Science Foundation under award number CCSS-1937460. Their support is gratefully acknowledged. Any opinions, findings, and conclusions or recommendations expressed in this material are those of the authors and do not necessarily reflect the views of the sponsors. The author(s) declared no potential conflicts of interest with respect to the research, authorship, and/or publication of this article.

References

[1] J. Hong, S. Laflamme, J. Dodson, B. Joyce, Introduction to state estimation of high-rate system dynamics, Sensors 18 (2018) 217, https://doi.org/10.3390/s18010217.
[2] J. Dodson, B. Joyce, J. Hong, S. Laflamme, J. Wolfson, Microsecond state monitoring of nonlinear time-varying dynamic systems, in: Volume 2: Modeling, Simulation and Control of Adaptive Systems Integrated System Design and Implementation Structural Health Monitoring, American Society of Mechanical Engineers, 2017. doi: 10.1115/smasis2017-3999..
[3] J. Hong, S. Laflamme, L. Cao, J. Dodson, B. Joyce, Variable input observer for nonstationary high-rate dynamic systems, Neural Computing and Applications (2018), https://doi.org/10.1007/s00521-018-3927-x.
[4] A. Prudhom, J. Antonino-Daviu, H. Razik, V. Climente-Alarcon, Time-frequency vibration analysis for the detection of motor damages caused by bearing currents, Mechanical Systems and Signal Processing 84 (2017) 747–762, https://doi.org/10.1016/j.ymssp.2015.12.008.
[5] Y. Bao, Z. Shi, J.L. Beck, H. Li, T.Y. Hou, Identification of time-varying cable tension forces based on adaptive sparse time-frequency analysis of cable vibrations, Structural Control and Health Monitoring 24 (2016), https://doi.org/10.1002/stc.1889 e1889.
[6] C.D. Zhang, Y.L. Xu, Structural damage identification via multi-type sensors and response reconstruction, Structural Health Monitoring: An International Journal 15 (2016) 715–729, https://doi.org/10.1177/1475921716659787.
[7] S.E. Azam, E. Chatzi, C. Papadimitriou, A dual kalman filter approach for state estimation via output-only acceleration measurements, Mechanical Systems and Signal Processing 60–61 (2015) 866–886, https://doi.org/10.1016/j.ymssp.2015.02.001.
[8] E.N. Chatzi, A.W. Smyth, Particle filter scheme with mutation for the estimation of time-invariant parameters in structural health monitoring applications, Structural Control and Health Monitoring 20 (2012) 1081–1095, https://doi.org/10.1002/stc.1520.
[9] M.F. Shamsudin, C. Mares, C. Johnston, Y. Lage, G. Edwards, T.-H. Gan, Application of bayesian estimation to structural health monitoring of fatigue cracks in welded steel pipe, Mechanical Systems and Signal Processing 121 (2019) 112–123, https://doi.org/10.1016/j.ymssp.2018.11.004.
[10] F. Cadini, C. Sbarufatti, M. Corbetta, M. Giglio, A particle filter-based model selection algorithm for fatigue damage identification on aeronautical structures, Structural Control and Health Monitoring 24 (2017), https://doi.org/10.1002/stc.2002 e2002.
[11] R. Kumar, P. Syam, S. Das, A.K. Chattopadhyay, Review on model reference adaptive system for sensorless vector control of induction motor drives, IET Electric Power Applications 9 (2015) 496–511, https://doi.org/10.1049/iet-epa.2014.0220.
[12] E. Kayacan, T.I. Fossen, Feedback linearization control for systems with mismatched uncertainties via disturbance observers, Asian Journal of Control 21 (2018) 1064–1076, https://doi.org/10.1002/asjc.1802.
[13] X. Zhang, Z. Li, Sliding-mode observer-based mechanical parameter estimation for permanent magnet synchronous motor, IEEE Transactions on Power Electronics 31 (2016) 5732–5745, https://doi.org/10.1109/tpel.2015.2495183.
[14] B. Joyce, J. Dodson, S. Laflamme, J. Hong, An experimental test bed for developing high-rate structural health monitoring methods, Shock and Vibration (2018) 1–10, https://doi.org/10.1155/2018/3827463.
[15] A. Downey, J. Hong, J. Dodson, M. Carroll, J. Scheppegrell, Millisecond model updating for structures experiencing unmodeled high-rate dynamic events, Mechanical Systems and Signal Processing 138 (2020), https://doi.org/10.1016/j.ymssp.2019.106551 106551.
[16] J. Yan, X. Du, S. Laflamme, L. Leifsson, C. Hu, A. Chen, Model-assisted validation of a strain-based dense sensor network, in: K.-W. Wang, H. Sohn, H. Huang, J.P. Lynch (Eds.), Sensors and Smart Structures Technologies for Civil, Mechanical, and Aerospace Systems 2019, SPIE, 2019. doi: 10.1117/12.2515232..
[17] K.S. Narendra, A.M. Annaswamy, Persistent excitation in adaptive systems, International Journal of Control 45 (1987) 127–160, https://doi.org/10.1080/00207178708933715.
[18] B.S. Joyce, J. Hong, J.C. Dodson, J.C. Wolfson, S. Laflamme, Adaptive observers for structural health monitoring of high-rate, time-varying dynamic systems, in: Structural Health Monitoring, Photogrammetry & DIC, vol. 6, Springer International Publishing, 2018, pp. 109–119. doi: 10.1007/978-3-319-74476-6_16..
[19] E. Lavretsky, K.A. Wise, Robust and Adaptive Control, Springer London, 2013, https://doi.org/10.1007/978-1-4471-4396-3.
[20] G. Chowdhary, E. Johnson, Concurrent learning for convergence in adaptive control without persistency of excitation, in: 49th IEEE Conference on Decision and Control (CDC), IEEE, 2010, https://doi.org/10.1109/cdc.2010.5717148.
[21] E. Kayacan, S. Park, C. Ratti, D. Rus, Online system identification algorithm without persistent excitation for robotic systems: Application to reconfigurable autonomous vessels, 2019.
[22] R. Kamalapurkar, N. Fischer, S. Obuz, W.E. Dixon, Time-varying input and state delay compensation for uncertain nonlinear systems, IEEE Transactions on Automatic Control 61 (2016) 834–839, https://doi.org/10.1109/tac.2015.2451472.
[23] Z.-Q. Qu, Model Order Reduction Techniques with Applications in Finite Element Analysis, Springer Science & Business Media, 2013.

[24] A. Cancelli, S. Laflamme, A. Alipour, S. Sritharan, F. Ubertini, Vibration-based damage localization and quantification in a pretensioned concrete girder using stochastic subspace identification and particle swarm model updating, Structural Health Monitoring (2019), https://doi.org/10.1177/1475921718820015, 147592171882001.
[25] S. Boyd, S. Sastry, Necessary and sufficient conditions for parameter convergence in adaptive control, Automatica 22 (1986) 629–639, https://doi.org/10.1016/0005-1098(86)90002-6.
[26] G. Chowdhary, T. Yucelen, M. Mühlegg, E.N. Johnson, Concurrent learning adaptive control of linear systems with exponentially convergent bounds, International Journal of Adaptive Control and Signal Processing 27 (2012) 280–301, https://doi.org/10.1002/acs.2297.
[27] R. Kamalapurkar, B. Reish, G. Chowdhary, W.E. Dixon, Concurrent learning for parameter estimation using dynamic state-derivative estimators, IEEE Transactions on Automatic Control 62 (2017) 3594–3601, https://doi.org/10.1109/tac.2017.2671343.
[28] G. Chowdhary, E. Johnson, A singular value maximizing data recording algorithm for concurrent learning, in: Proceedings of the 2011 American Control Conference, IEEE, 2011, https://doi.org/10.1109/acc.2011.5991481.
[29] J. Hong, S. Laflamme, L. Cao, B. Joyce, J. Dodson, Hybrid algorithm for structural health monitoring of high-rate systems, in: Volume 2 - Mechanics and Behavior of Active Materials, American Society of Mechanical Engineers, 2018. doi: 10.1115/smasis2018-7977..